Geoscience Frontiers 12 (2021) 101246

Contents lists available at ScienceDirect

Geoscience Frontiers

journal homepage: www.elsevier.com/locate/gsf

Research Paper

The deep mantle upwelling beneath the northwestern South China Sea: Insights from the time-varying residual subsidence in the Qiongdongnan Basin

Zhong-Xian Zhao [a,b,c,d,*]

[a] Key Laboratory of Ocean and Marginal Sea Geology, South China Sea Institute of Oceanology, Innovation Academy of South China Sea Ecology and Environmental Engineering, Chinese Academy of Sciences, Guangzhou 511458, China
[b] Laboratory for Marine Mineral Resources, Qingdao National Laboratory for Marine Science and Technology, Qingdao 266237, China
[c] Southern Marine Science and Engineering Guangdong Laboratory, Guangzhou 511458, China
[d] Key Laboratory of Marine Mineral Resources, Ministry of Natural Resources, Guangzhou 510760, China

ARTICLE INFO

Article history:
Received 28 October 2020
Revised 19 May 2021
Accepted 2 June 2021

Handling Editor: M. Yoshida

Keywords:
Residual subsidence
Deep mantle upwelling
Strain rate
Qiongdongnan Basin
Northwestern South China Sea margin

ABSTRACT

Deep hot mantle upwelling is widely revealed around the Qiongdongnan Basin on the northwestern South China Sea margin. However, when and how it influenced the hyper-extended basin is unclear. To resolve these issues, a detailed analysis of the Cenozoic time-varying residual subsidence derived by subtracting the predicted subsidence from the backstripped subsidence was performed along a new seismic reflection line in the western Qiongdongnan Basin. For the first time, a method is proposed to calculate the time-varying strain rates constrained by the faults growth rates, on basis of which, the predicted basement subsidence is obtained with a basin- and lithosphere-scale coupled finite extension model, and the backstripped subsidence is accurately recovered with a modified technique of backstripping to eliminate the effects of later episodes of rifting on earlier sediment thickness. Results show no residual subsidence in 45–28.4 Ma. But after 28.4 Ma, negative residual subsidence occurred, reached and remained ca. −1000 m during 23–11.6 Ma, and reduced dramatically after 11.6 Ma. In the *syn*-rift period (45–23 Ma), the residual subsidence is ca. −1000 m, however in the post-rift period (23–0 Ma), it is positive of ca. 300 to 1300 m increasing southeastwards. These results suggest that the *syn*-rift subsidence deficit commenced at 28.4 Ma, while the post-rift excess subsidence occurred after 11.6 Ma. Combined with previous studies, it is inferred that the opposite residual subsidence in the syn- and post-rift periods with similar large wavelengths (>10^2 km) and km-scale amplitudes are the results of transient dynamic topography induced by deep mantle upwelling beneath the central QDNB, which started to influence the basin at ca. 28.4 Ma, continued into the Middle Miocene, and decayed at ca. 11.6 Ma. The initial mantle upwelling with significant dynamic uplift had precipitated considerable continental extension and faulting in the Late Oligocene (28.4–23 Ma). After ca. 11.6 Ma, strong mantle upwelling probably occurred beneath the Leizhou–Hainan area to form vast basaltic lava flow.

1. Introduction

The classic stretching models have provided quantitative frameworks for predicting lithospheric isostatic subsidence of rifted basins or margins (Mckenzie, 1978; Jarvis and McKenzie, 1980). However, the backstripped subsidence is usually significantly larger or smaller than the predicted subsidence, such as in the NW European passive margin (Praeg et al., 2005), the North Sea and Faeroe-Shetland basins (Nadin et al., 1997), the Songliao Basin (Li and Liu, 2015), and the south and northeast Australian margins (Müller et al., 2000; Brown et al., 2001). One reason is that, in addition to the lithospheric isostatic subsidence, the rifted basins or margins also recorded the dynamic topography induced by the deep mantle viscous flow possibly due to ocean spreading (Praeg et al., 2005), slab subduction (Müller et al., 2000; Brown et al., 2001; Li and Liu, 2015) or mantle plume (Nadin et al., 1997). Thus, the time-varying residual subsidence, derived by sub-

* Address: Key Laboratory of Ocean and Marginal Sea Geology, South China Sea Institute of Oceanology, Innovation Academy of South China Sea Ecology and Environmental Engineering, Chinese Academy of Sciences, Guangzhou 511458, China.
E-mail address: zxzhao@scsio.ac.cn

https://doi.org/10.1016/j.gsf.2021.101246
1674-9871/

tracting the predicted subsidence from the backstripped subsidence, can provide new insights into the variation of the dynamic topography and the deep mantle processes (Wheeler and White, 2000).

However, some issues still exist in the current methods to calculate the true backstripped and predicted subsidence of rifted basins (Jarvis and McKenzie, 1980; Sclater and Christie, 1980; Zhao et al., 2013). Sediment deposited in earlier periods were usually stretched and thinned by later episodes of rifting, but the process is not considered in the routine method of backstripping (Sclater and Christie, 1980; Zhao et al., 2013), leading to significant underestimation of the recovered *syn*-rift sediment thickness and tectonic subsidence. The predicted subsidence by the lithospheric finite extension model is, however, highly dependent on the time-varying strain rates (Jarvis and McKenzie, 1980), but the current methods cannot give accurate, subsidence-independent strain rates that also comply with the multiple rifting background, such as that inversed from the backstripped subsidence (White, 1994; Xie et al., 2006), measured from faults heaves (Davis and Kusznir, 2004; Reston, 2009) and the average strain rates derived by dividing the total strain (whole crustal extension factor) by the duration of the *syn*-rift period (Shi et al., 2017; Zhao et al., 2018a).

As faults are highly sensitive to regional stress, the fault growth rates are one best indicator of the multiple episodes of rifting. Thus, we attempt to use fault growth rates as weight to allocate the total strain (whole crustal extension factor) to derive the time-varying strain rates, based on which, we forward predict the basement subsidence. Then we also propose a modified technique of backstripping by incorporating the time-varying strain rates into the routine method (Sclater and Christie, 1980; Zhao et al., 2013) to eliminate the effects of later episodes of rifting. Thus, the residual subsidence can be obtained accurately by subtracting the predicted subsidence from the backstripped subsidence. Here, these methods are applied to the rifted Qiongdongnan Basin (QDNB) on the northwestern South China Sea margin, where active mantle upwelling occurred in the late Cenozoic indicated by the extensive eruption of the OIB-type volcanism (Hoang and Flower, 1998; Yan and Shi, 2008; Xu et al., 2012; Wang et al., 2013), the high mantle temperature (Hoang and Flower, 1998; Wang and Huang, 2012; Wang et al., 2012; Huang et al., 2015; Wei and Chen, 2016; Yang et al., 2019) and the broad low seismic velocity in the upper mantle (Huang and Zhao, 2006; Montelli et al., 2006; Zhao, 2007; Lei et al., 2009; Xia et al., 2016), but when and how the deep mantle upwelling influenced the QDNB is unclear. Moreover, the *syn*-rift subsidence deficit (Shi et al., 2017; Zhao et al., 2018a) and the post-rift accelerated subsidence (Xie et al., 2006; Zhao et al., 2013, 2018b) of the QDNB have been revealed, but the exact time of the subsidence deficit is unknown, and the mechanism of the subsidence anomaly is still debated (Xie et al., 2006; Zhao et al., 2013, 2018a, 2018b; Shi et al., 2017). Here, these issues are attempted to be resolved by using the new methods with a newly released seismic reflection line.

2. Geological settings

The South China Sea is one of the largest Cenozoic marginal basins in the western Pacific region. It was formed in a complex tectonic setting interacted by the Eurasian, Pacific and Indian-Australian plates, and is semi-circled by several large active subduction belts, including Indo-Australian subduction-collision in the south and west and the Philippine-Pacific slabs in the east (Cullen et al., 2010). The initial rifting in the South China Sea probably started in the latest Cretaceous to early Paleocene when a Mesozoic convergent margin changed to extension (Su et al., 1989; Clift and Lin, 2001; Franke et al., 2014). After multi-stage rifting (Ru and Pigott, 1986; Clift et al., 2001; Lei et al., 2019, 2020), the continent first broke up and the eastern South China Sea basin opened in the Early Oligocene (Briais et al., 1993; Li et al., 2014; Sun et al., 2018). Then the seafloor spreading jumped southwards and propagated to the SW South China Sea basin in the Late Oligocene–Early Miocene (Briais et al., 1993; Li et al., 2014; Ding et al., 2018). Several prolific petroleum basins were developed on the northern South China Sea margin, such as the NE-trending Pearl River Mouth Basin and the QDNB (Fig. 1a). The QDNB is located in the northwestern South China Sea margin (Fig. 1), and pretty close to the Hainan Island with a water depth of ca. 100 to 2800 m (Fig. 1b). Regionally, the Basin is surrounded by the offshore Red River fault and the NW-elongated Yinggehai–Song Hong basin to the west, by the Shenhu Uplift and the Pearl River Mouth Basin to the northeast, by Hainan Island to the north and by Xisha block to the south (Fig. 1a). Further southwards, it is the Phu Khanh Basin and the SW South China Sea basin (Fig. 1a). In the late Cenozoic, voluminous and extensive OIB-type basalts have erupted around the QDNB in the Leizhou–Hainan area, the Indochina peninsula and the South China Sea basin, suggesting strong mantle dynamics beneath the Hainan Island (Wang et al., 2013).

The continental crust in the QDNB has been hyperextended (Zhang et al., 2008; Qiu et al., 2013; Zhao et al., 2015a; Lei and Ren, 2016) with three structural units formed from NW to SE (Fig. 1b), the northern depression, the central depression, and the southern uplift. The central depression comprises of the LDS, LSS, SNS, BDS, and CCS (Fig. 1b). The western QDNB mainly comprises asymmetric half grabens and fault blocks, in contrast, the eastern QDNB consists of symmetric grabens (Zhao et al., 2015a). Rifting and faulting in the QDNB started at ca. 45 Ma, was strongly active in the Late Oligocene (Clift and Sun, 2006; Zhao et al., 2018b), and ceased at ca. 23 Ma (Zhao et al., 2018b). During the *syn*-rift period, faults formed and trended in NE-SW, E-W and NW-SE orientations (Fig. 1b). Seismic interpretations indicate that the activities of these faults were generally ceased at ca. 23 Ma (Fig. 2). In the post-rift period, the basin underwent a regional slow subsidence in the Early-Middle Miocene and a rapid subsidence since the Late Miocene (Xie et al., 2006; Zhao et al., 2013, 2018b). It was lacustrine deposition occurring in the Eocene, marine-continent transitional environment in the Oligocene, littoral to neritic environment in the Early and Middle Miocene, and a deep marine since the Late Miocene (Xie et al., 2008; Su et al., 2011; Zhao et al., 2018b).

3. Data and methods

3.1. Seismic reflection data

A new composite deep seismic reflection line 1 in the western QDNB is studied (Fig. 1b), which is located ca. 45 km to the east of the seismic line 2 used by Zhao et al. (2018a). The seismic line has a total length of 217 km, extending across the northern depression, the central depression and the southern uplift (Fig. 1b). The composite seismic profile was acquired by the China National Offshore Oil Corporation (CNOOC) in 2006 and 2011 through 648 channels, 8.1 km-long streamer, and were recorded in SEG-D format at 2 ms sampling intervals and 12 s trace length. Along the high resolution seismic profile, the sedimentary sequences, the reflective basement, and the deep Moho are well imaged (Fig. 2). For the sedimentary layer, 16 sequence boundaries (S100 (45 Ma), S80 (33.9 Ma), S72 (31.5 Ma), S71 (29.9 Ma), S70 (28.4 Ma), S62 (25.5 Ma), S61 (23.8 Ma), S60 (23 Ma), S52 (18.3 Ma), S50 (16 Ma), S41 (13.4 Ma), S40 (11.6 Ma), S31 (8.2 Ma), S30 (5.5 Ma), S29 (4.2 Ma), and seabed (0 Ma)) are interpreted and provided by the CNOOC with their ages determined on

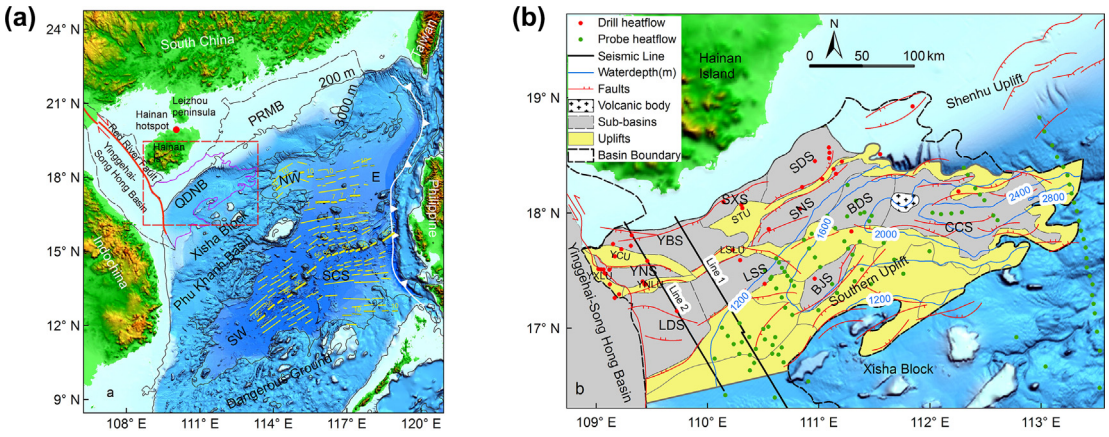

Fig. 1. (a) Tectonic units of the South China Sea region with bathymetric contours of 200 and 3000 m, modified from Zhao et al. (2018a). The South China Sea has three sub-basins, the E sub-basin, the NW sub-basin and the SW sub-basin with the overlapped magnetic isochrones (dashed yellow lines) (Briais et al., 1993). The white triangles are subduction or collision zones, the red point is Hainan hotspot, and the dashed red rectangle outlines the Qiongdongnan Basin. QDNB, Qiongdongnan Basin; PRMB, Pearl River Mouth Basin; SCS, South China Sea. (b) Structural unit of the QDNB (see location in Fig. 1a) with a SE-tilted seafloor shown by bathymetric contours (unit in meters), modified from Zhao et al. (2018a). The extensional faults are basin-widely distributed (red lines) and a volcanic body extruded between the Baodao and Changchang Sub-basins. The composite seismic reflection line 1 in black line is located in the western QDNB, ca. 45 km to the east of the seismic line 2 used by Zhao et al. (2018a). The heat flow data measured from the drill sites are in red points, and those measured from the seafloor heat flow probe stations are in green points (Wang et al., 2014). YNS, Yacheng Nan Sub-basin; YBS, Yacheng Bei Sub-basin; SXS, Songtao Xi Sub-basin; SDS, Songtao Dong Sub-basin; LDS, Ledong Sub-basin; LSS, Liushui Sub-basin; SNS, Songtao Nan Sub-basin; BDS, Baodao Sub-basin; CCS, Changchang Sub-basin; BJS, Beijiao Sub-basin.

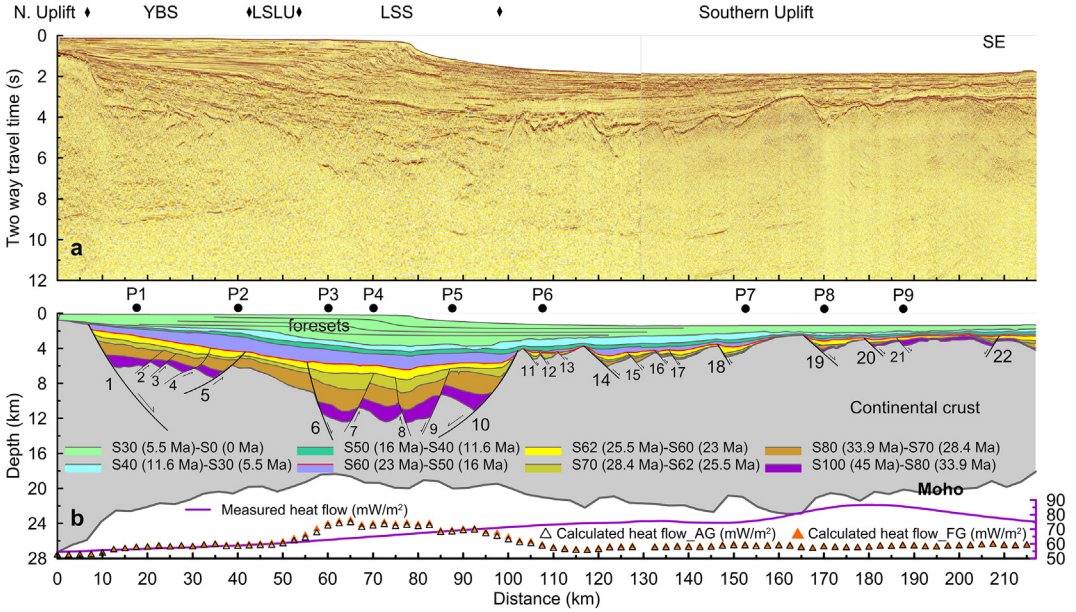

Fig. 2. (a) The composite deep seismic reflection profile acquired by the CNOOC in 2006 and 2011 (see location in Fig. 1b). (b) The depth profile with stratigraphic and structural interpretation. The faults are numbered. The red line is the marked unconformity at the end of the *syn*-rift period (23 Ma). The thick, gray line is the Moho. The purple line is the measured heat flow progressively rising from 55 to 87 W/m^2 toward the SE end (Wang et al., 2014; Shi et al., 2015). The black triangles are the calculated heat flow using the finite extension model based on the average strain rates while the orange triangle is that based on the faults growth rates weighted strain rates. P1-P9 are selected points for detailed subsidence analysis.

basis of biostratigraphic analysis (Zhao et al., 2018b), nine of which are shown in Fig. 2. The Moho discontinuities are clearly featured by the reflections of medium continuity, low frequency and large amplitude at the TWT of ca. 8–10 s (Fig. 2a).

3.2. Gravity modeling

The crustal thickness along line 1 is determined by both the seismic reflection Moho and gravity modelling (Fig. 3). The sedimentary basement and the crust-mantle boundary (Moho) are clearly imaged from the reflection seismic profile 1 (Fig. 2). The thickness of the remnant crust between the top basement and the Moho reflection (Fig. 2), is first roughly determined by multiplying the TWT with an average continental crust P-wave velocity of 6.5 km/s (Christensen and Mooney, 1995). Results show that the crust thickness is ca. 6 to 26.5 km with the thinnest part in the LSS (Fig. 2b). Gravity modeling is also performed to reassess the crust structures (Fig. 3). The free-air gravity anomalies along line 1 is ca. −50 to 20 mGal (Sandwell et al., 2014) (Fig. 3d). It is ca. −20–0 mGal in the YBS, increases progressively to ca. 20 mGal in the LSS, then reduces significantly to a broad negative range of ca. −50 and −30 mGal for most of the southern uplift (Fig. 3d). The

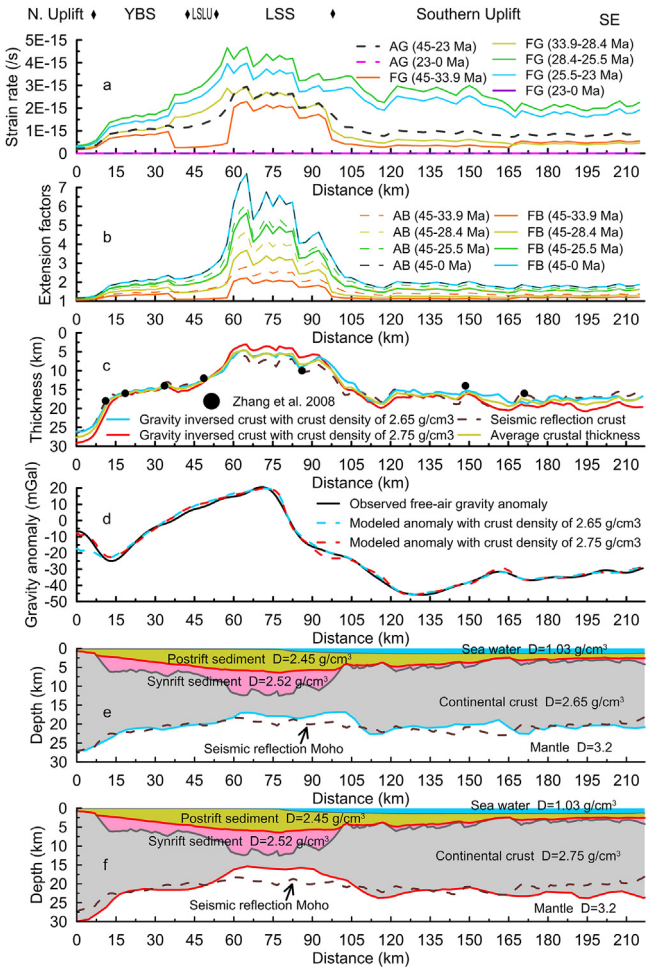

Fig. 3. (a) The faults growth rates weighted strain rates (FG) derived by utilizing the faults growth rates as weight to allocate the total strain (whole crust extension factor), and the average strain rates (AG) by assuming uniform faults growth rates during the *syn*-rift period. (b) The extension factors calculated by integrating the faults growth rates weighted strain rates with time (FB) and the average strain rates with time (AB). (c) The seismically interpreted, the gravity inversed and their average crustal thickness. The black dots are crustal thickness from Zhang et al. (2008). (d) The observed and modeled free-air gravity anomaly. The observed gravity is from 1 arc-minute resolution new global marine gravity V27.1 (Sandwell et al., 2014), with the overall value of ca. −50to 20 mGal. (e) The gravity model using the bulk crust density of 2.65 g/cm^3. (f) The gravity model using the bulk crust density of 2.75 g/cm^3.

occurrence of the large positive anomaly in the LSS and the dramatic reduction southwards may be the so-called 'edge-effect' related to the shelf break (Watts and Stewart, 1998) (Fig. 3d). The initial model for gravity modeling contains the layers of the sea-water, the syn- and post-rift sediment, which are interpreted from the reflection seismic profile (Fig. 2b), converted from time to depth (Fig. 2b) using the Vertical Seismic Profile (VSP) data (Zhao et al., 2015b, 2018b), and remain fixed during all the following adjustment (Fig. 3e and 3f). In reference to previous gravity models (Qiu et al., 2013), their densities are set to 1.03, 2.45 and 2.52 g/cm^3, respectively. The density for the sub-sedimentary crust is given 2.65 and 2.75 g/cm^3, respectively, in two separate models (Fig. 3e and 3f). Thus, through repeatedly modifying the thickness of the crust layer, the modeled and observed gravity anomalies are finally well fitted. Then the modeled crustal structures are shown in Fig. 3e and 3f, respectively. Except the LSS along line 1, the gravity modeled Moho depth and crust thickness using the bulk crust density of 2.75 g/cm^3 are apparently larger than the seismically interpreted (Fig. 3f), while that using the bulk crust density of 2.65 g/cm^3 are very close to the seismically interpreted (Fig. 3e). Beneath the LSS, the gravity inversed Moho depth and crustal thickness is, however, smaller than seismically interpreted (Fig. 3c, 3e and 3f), which might be caused by the improper setup of the sediment density in the basin. The sediment in the LSS is ca. 12 km thick and the density should increases with burial depth as porosity reduces under compaction. Thus the lower sediment layer must be much heavier than assumed. Compared with previous gravity derived crustal thickness (Zhang et al., 2008), our result show ca. 1–3 km thicker or thinner in the LSS and southern uplift, however, the overall trend is identical (Fig. 3c). The whole crustal extension factors (β_{wc}) along line 1 (Fig. 3b) is derived as the ratio of the initial crustal thickness of 32 km (Nissen and Hayes, 1995; Nissen et al., 1995) to the present average crustal thickness of the seismically interpreted and the gravity modelled (Fig. 3c).

3.3. The faults growth rates weighted strain rates

Faults are highly sensitive to regional stress, and the multiple rifting history in the QDNB is well manifested by the faults growth rates with the strong fault activity in the late Oligocene indicating an episode of fast crustal stretching (Zhao et al., 2018b). Along line 1, we have interpret 22 pieces of faults (Fig. 2) and calculated the faults growth rates as the thickness differences between the equivalent strata in the hanging wall and footwall divided by the corresponding time span (Table 1). Using the average fault growth rates of these faults (Table 1) as weight to allocate the total strain (whole crustal extension factor), we obtain the faults growth rates weighted strain rates (Fig. 3a) with Eq. (1), which is modified from the relationship among the extension factor, strain rate and time (Jarvis and McKenzie, 1980; White, 1994). We also calculate the average strain rates (Fig. 3a) by assuming uniform faults growth rates during the *syn*-rift period in Eq. (1). Then the extension factors at each time (Fig. 3b) can be derived by integrating the strain rates with time using Eq. (2).

$$G_i = \ln\beta_{wc} \Big/ \left(\sum_{i=1}^{n} f_i \cdot \Delta t_i\right) \cdot f_i \tag{1}$$

$$\beta_i = \exp\left(\sum_{i=1}^{n} G_i(t) \cdot \Delta t_i\right) \tag{2}$$

where, β_{wc} is the whole crustal extension factors, n is the number of strata, Δt_i is the time span of stratum i, f_i is the faults growth rate of stratum i, G_i is the faults growth rates weighted strain rates of stratum i, β_i is the extension factor at the end time of stratum i.

3.4. The modified technique of backstripping

The basement tectonic subsidence recorded by strata in sedimentary basins is usually derived through backstripping by decompacting the buried sediment, removing the load effect, and correcting the base level under local isostasy (Sclater and Christie, 1980; Zhao et al., 2013). In rifted basins, the strata formed in earlier rifting periods are usually stretched and thinned many times by later episodes of rifting, however, these processes have not been coupled in the routine backstripping method, which yields significant underestimation of the recovered *syn*-rift sediment thickness and tectonic subsidence (Eq. (3)) (Zhao et al., 2013). Thus, it is necessary and essentially important to modify the routine method of backstripping by taking the multiple extension into account. Here, we give a modified Eq. (4) to resolve this issue by incorporating the time-varying extension factors (Fig. 3b) into the routine method (Sclater and Christie, 1980;

Table 1
The faults growth rates (m/Ma) along line 1.

	45–33.9 Ma	33.9–28.4 Ma	28.4–25.5 Ma	25.5–23 Ma	23–0 Ma
F1	120.8	283.5	236.2	232.0	–
F4	9.8	16.2	58.0	29.6	–
F5	70.7	82.4	57.7	46.2	–
F6	125.9	85.5	201.2	26.7	–
F7	43.1	62.0	271.5	–	–
F8	35.9	83.6	88.7	–	–
F9	122.1	99.5	205.4	–	–
F10	178.3	339.8	370.4	200.5	–
F14	–	121.7	109.9	181.0	–
F15	–	60.4	26.4	55.1	–
F16	–	–	–	78.3	–
F17	–	–	–	54.9	–
F18	–	43.6	67.6	317.6	–
F19	31.5	55.5	–	231.5	–
F20	22.2	29.2	–	140.6	–
Average	71.1	90.0	145.7	123.8	0

Zhao et al., 2013). The modified technique of backstripping not only can decompact the deep buried sequence, but also can recover its original thickness by eliminating the effects of later episodes of rifting, which is thus applied to calculate the sediment thickness (Fig. 4) and the 1D unloaded tectonic subsidence (Fig. 5) along line 1.

$$EBS_i = ST_i \times \frac{\rho_m - \rho_s}{\rho_m} + PWD_i \times \frac{\rho_m - \rho_w}{\rho_m} - \Delta BL_i \quad (3)$$

$$EBS_i = \frac{\beta_{wc}}{\beta_i} \times ST_i \times \frac{\rho_m - \rho_s}{\rho_m} + PWD_i \times \frac{\rho_m - \rho_w}{\rho_m} - \Delta BL_i \quad (4)$$

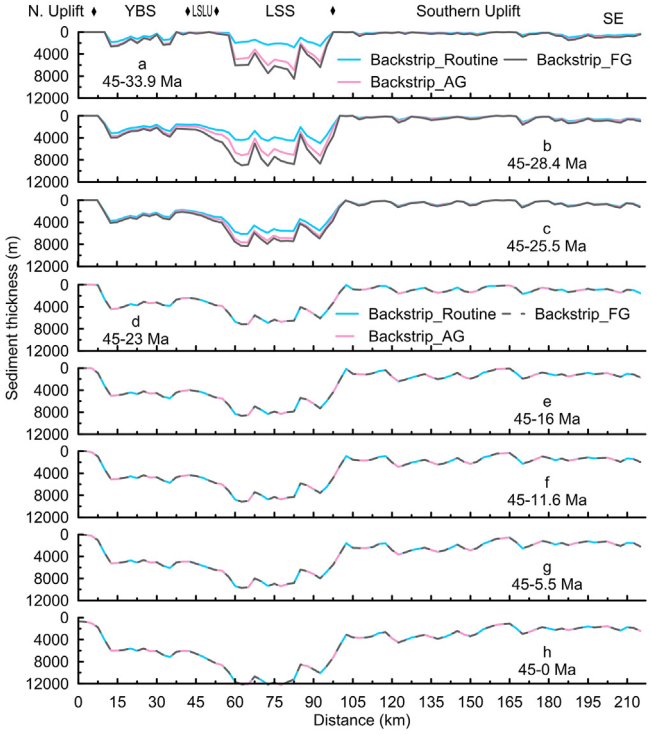

Fig. 4. The recovered sediment thickness with the routine method of backstripping (Backstrip_Routine), and the modified technique of backstripping based on the average strain rates (Backstrip_AG) and the faults growth rates weighted strain rates (Backstrip_FG). Huge differences appear in the *syn*-rift periods (45–23 Ma) in the LSS where the Eocene and early Oligocene sediment is preserved (Fig. 2) and large multiple extension occurred (Fig. 3a and 3b).

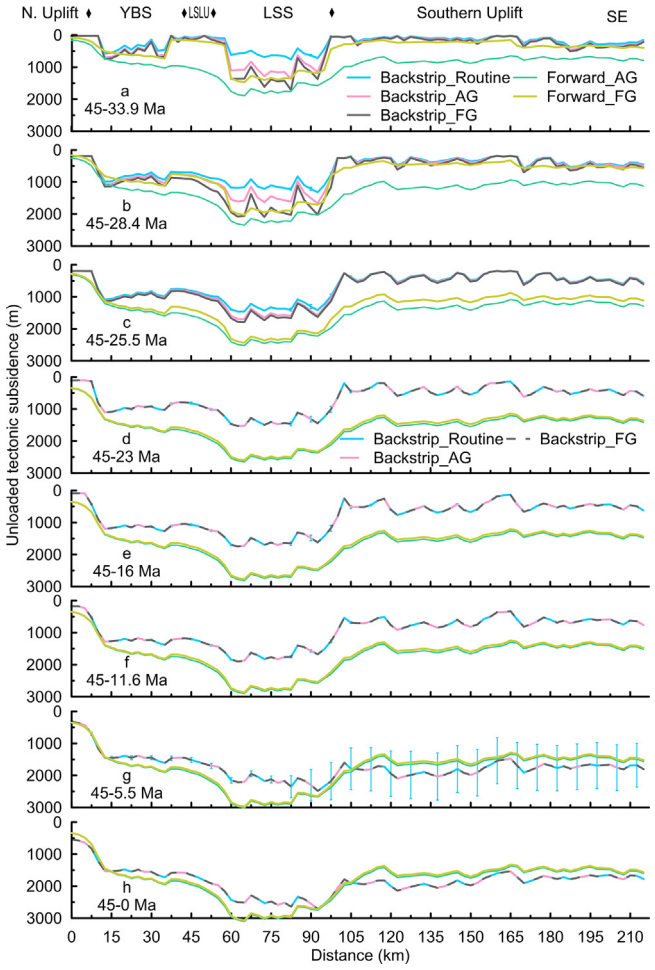

Fig. 5. The unloaded tectonic subsidence calculated through backstripping and forward modelling. Three methods are used in obtaining the backstripped subsidence: the routine method of backstripping (Backstrip_Routine), the modified technique of backstripping based on the average strain rates (Backstrip_AG) and the fault growth rates weighted strain rates (Backstrip_FG). The forward modelled subsidence is derived on basis of the average strain rates (Forward_AG) and the faults growth rates weighted strain rates (Forward_FG). The blue vertical bars are the uncertainties in water depth.

where ρ_w, ρ_s, and ρ_m are the average density of water (1030 kg/m^3), sediment and mantle (3184 kg/m^3), respectively. β_{wc} is the whole crustal extension factor, and β_i is the extension factor at time *i*.

EBS_i, ST_i, PWD_i and ΔBL_i is the unloaded tectonic subsidence, decompacted sediment thickness, paleo-water depth and the variation of the base level at time *i*.

In the QDNB, the hyper-extended crust (Figs. 2 and 3) and the high heat flow (85–105 mW/m^2) (Wang et al., 2014; Shi et al., 2017) suggest that the lithosphere is sufficiently weak and it is reasonable to assume local isostasy in conducting backstripping (Clift et al., 2002; Wang et al., 2014; Shi et al., 2017). The parameters used in the backstripping, such as the lithology of each sequence, the local exponentially porosity-depth relations, the paleo-water depth and the base levels, were thoroughly and carefully analyzed and determined in our previous studies (Zhao et al., 2015b, 2018b). Since the paleo-water depth has a large effect on the calculated subsidence, its uncertainty is shown in Fig. 5. As the *syn*-rift sedimentary environment in the Late Eocene to Oligocene is dominated by lacustrine, marsh, coastal plain, and littoral facies (Zhao et al., 2018b), the uncertainty in the paleo-water depth is less than 100 m (Fig. 5). In the post-rift periods, it is littoral to neritic environment in the Early-Middle Miocene and a shelf-slope, bathyal-abyssal environment since the Late Miocene (Xie et al., 2008; Su et al., 2011; Zhao et al., 2018b), the largest uncertainty is ca. 200, 200 and 750 m at 16, 11.6 and 5.5 Ma, respectively (Fig. 5), which are less than the amount of the tectonic subsidence and do not significantly affect the subsidence analysis (Fig. 5).

3.5. Forward modeling

In rifted basins or margins, the lithospheric isostatic tectonic subsidence is mainly contributed by lithospheric thinning and thermal cooling (Mckenzie, 1978; Jarvis and McKenzie, 1980), which can be predicted using a 1D uniform finite extension model (Jarvis and McKenzie, 1980; White, 1994). Considering the huge sediment thickness along line 1 in the QDNB (ca. 12 km, Fig. 4), and its effect of sediment thermal blanketing and radioactive heat generation on the basement subsidence and heat flow, we decide to utilize a 1D basin- and lithosphere-scale coupled finite extension model (Eqs. (5)–(7)) to predict the unloaded tectonic subsidence and the heat flow on basis of the time-varying strain rates (Fig. 3a). As previous studies (Rüpke et al., 2008; Theissen and Rupke, 2010), the model here allows for multiple finite stretching given the strain rate history (White, 1994), and can simultaneously resolves the basin-scale processes (deposition, compaction, stretching, and heat transfer) and the lithosphere-scale processes (stretching, heat transfer, and local isostatic response).

$$\rho \cdot c_p \cdot \left(\frac{\partial T}{\partial t} + G(t)(a-z)\frac{\partial T}{\partial z}\right) = \frac{\partial}{\partial z}\left(k\frac{\partial T}{\partial z}\right) + H\nu \tag{5}$$

$$S(t) = A(1 - 1/\beta) - BQ(t) \tag{6}$$

$$q = -k\frac{\partial T}{\partial z} \tag{7}$$

where, ρ,c_p,T,t,G,a,z,k,$H\nu$, $S(t)$and q are the density, specific heat, temperature, time, strain rate, lithosphere thickness, depth, thermal conductivity, radiogenic heat generation, unloaded tectonic subsidence and heat flow, respectively. The density is obtained using a linear relation $\rho = \rho_0(1 - \alpha T)$, where ρ_0 is the material density at 0 ℃ and α is the thermal expansion coefficient. $A = t_c(\rho_m - \rho_c)/\rho_a$, $B = \alpha \cdot \rho_m/\rho_a$, $Q(t) = \int_0^a [T(z,t) - T(z,\infty)]\mathrm{d}z$, where t_c is crustal thickness, ρ_c, ρ_m the crust and mantle density at 0 ℃, respectively, ρ_a the asthenosphere density at 1333 ℃, $T(z,t)$ is the temperature of the lithosphere as a function of depth and time, $T(z,\infty)$ is the equilibrium temperature structure of the lithosphere.

In the coupled model here, we set four layers of sediment, upper crust, lower crust, and mantle lithosphere (Table 2). When conduct the finite extensions using the time-varying strain rates (Fig. 3a), heat transfer occurs through advection and conduction to derive the time-varying temperature structure of the lithosphere by solving the 1D unsteady thermal diffusion Eq. (5). Then the unloaded tectonic subsidence can be calculated using Eq. (6) (Fig. 5), and the surface heat flow can be obtained through Eq. (7) (Fig. 2). For every time step, new sediment package is deposited and old sediments are compacted, the lithology and the compaction parameters are the same as that in the 1D backstripping. The feedback of the porosity on the sediment thermal conductivity is also considered (Theissen and Rupke, 2010). The top boundary temperature is fixed at 0 ℃ and the bottom boundary temperature at the base of lithosphere is 1333℃. The initial temperature is set to increase linearly from top to bottom. The largest thermal lithosphere thickness of ca. 110 km suggested by the thermal regime (Tang et al., 2014) is used as the initial lithospheric thickness here (Table 2). Meanwhile, we also tried thicker (120 km) and thinner (100 km) lithospheric thickness, which gives a little shallower or deeper basement, respectively. Other parameter values used here in reference to previous studies are listed in Table 2.

3.6. Calculation of the time-varying residual subsidence

Along line 1, the time-varying residual tectonic subsidence (Fig. 6) is derived by subtracting the predicted subsidence from the backstripped subsidence (Fig. 5), both of which are calculated based on the faults growth rates weighted strain rates. The residual subsidence provides us new insights into the variation of the dynamic topography and the deep mantle processes.

4. Results

4.1. The basin and crustal structure

The basin structure along line 1 resembles the previous result given in Zhao et al. (2018a). It is characterized by the lower faulted sub-basins and the upper sag sub-basin (Fig. 2), separated by a remarkable breakup unconformity (23 Ma), onto which most of the extensional faults are terminated (Fig. 2). In the YBS and LSS, faults have large offsets, penetrate deep into the basement (faults 1, 6 and 10) and thin the crust considerably (Fig. 2). The YBS is a large half graben controlled by the SE-dipping boundary fault 1 with a series of small antithetic faults formed in the hanging wall (Fig. 2). The LSS, bounded by large faults 6 and 10, is a ca. 50 km wide graben (Fig. 2). Within these half-grabens or grabens, thick Eocene-Oligocene *syn*-rift sediment was deposited and the lowest Eocene sediment was widely preserved (Fig. 2). In the southern uplift, the SE-dipping faults, however, have small offsets (faults 11–22), slightly thin the basement and yield distributed, small-scale half grabens, where only thin wedge-shaped sediment was deposited (Fig. 2). In the post-rift period, sediment was progressively overlying and onlapping the *syn*-rift sequences (Fig. 2). Particularly, the Pliocene sediment has occupied most of the post-rift basin space, and pushed the sedimentary shelf-break southeastward layer by layer (Fig. 2). The overall sediment thickness is ca. 6–12 km in the YBS and LSS, and only ca. 1.5–4 km in the southern uplift (Fig. 2). The largest sediment thickness is ca. 12 km occurring in the LSS, where the sub-sedimentary crust has been hyper-extended to ca. 5–6 km (Figs. 2 and 3c) with the crust extension factors of ca. 6 (Fig. 3b). Away from the LSS, the crust is less thinned, which is ca. 15 km thick in the YBS and ca. 15–21 km thick in the southern uplift (Figs. 2 and 3c). Correspondingly, the crust extension factor is ca. 2 in the YBS, and ca. 1.5–2 in the southern uplift (Fig. 3b). Unlike the crustal structure, the heat flow rises progressively from 55 to 87 W/m^2 toward the SE end (Fig. 2).

Table 2
Thermophysical parameters used in the modeling.

	Sediment layer	Upper crust	Lower crust	Lithospheric mantle
Initial thickness (km)	0	15	17	78
Density at 0 ℃ (kg/m^3)	2600	2700	2850	3330
Thermal expansion coefficient (℃$^{-1}$)	0	2.4e-5	2.4e-5	3.28e-5
Specific heat (J·kg^{-1}·℃$^{-1}$)	1050	1471	1392	1218
Heat generation (W·m^{-3})	1.0e-6	1.8e-6	0.5e-6	0
Thermal conductivity (W·m^{-1}·℃$^{-1}$)	1.3	2	2	3

Note: Parameters include the density and thermal expansion coefficient (McKenzie, 1978), the initial thickness (Tang et al., 2014), and the specific heat, heat generation and thermal conductivity (Theissen and Rupke, 2010; Shi et al., 2015, 2017).

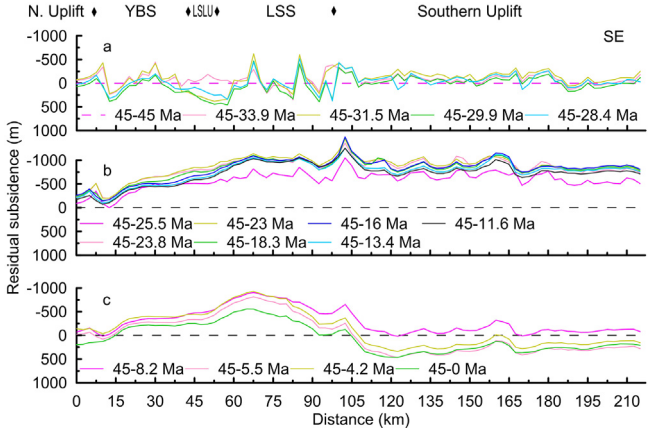

Fig. 6. The time-varying residual unloaded tectonic subsidence derived by subtracting the predicted subsidence from the backstripped subsidence, both of which, are calculated on basis of the faults growth rates weighted strain rates in Fig. 5.

4.2. The time-varying strain rates

Reliable strain rate is a requisite in rifted basins to understand the multiple episodes of rifting and to accurately calculate the tectonic subsidence through backstripping and forward modelling. Here, we interpret 22 pieces of faults along line 1 (Fig. 2), calculate the fault growth rates (Table1), and use them as weight to derive the time-varying strain rates and extension factors (Fig. 3a and 3b). The calculated average faults growth rates along line 1 are 71.1, 90, 145.7, 123.8 and 0 m/Ma in 45–33.9, 33.9–28.4, 28.4–25.5, 25.5–23 and 23–0 Ma, respectively (Table 1). The strongest fault activity in the Late Oligocene (28.4–23 Ma) and minor faults in the post-rift period (23–0 Ma) are consistent with previous studies (Zhao et al., 2018b). The Cenozoic time-varying strain rates along line 1 are between 0 and 4.5e-15 s^{-1} with the largest value in the Late Oligocene of 1e-15 to 3e-15, 3.5e-15 to 4e-15 and 2e-15 to 3e-15 s^{-1} in the YBS, LSS and southern uplift, respectively (Fig. 3a). By comparison with the strain rate inversed from the *syn*-rift tectonic subsidence (Xie et al., 2006), the calculated strain rate here is almost two times larger (Fig. 3a). We also calculate the average strain rate of the *syn*-rift period as previous studies (Shi et al., 2017; Zhao et al., 2018a), and it is 0.5e-15 to 1e-15, 2.5e-15 to 3e-15 and 1e-15 s^{-1} in the YBS, LSS and southern uplift, respectively (Fig. 3a). By integrating the strain rates with time, the calculated extension factor in the LSS is more than 2, 3, 4.5, and 6 at 33.9, 28.4, 25.5 and 0 Ma, respectively (Fig. 3b).

4.3. The backstripped sediment thickness and subsidence

The recovered sediment thickness using the routine method and the modified technique of backstripping are present in Fig. 4. Huge differences occur in the *syn*-rift periods (45–23 Ma, Fig. 4a-c), especially in the LSS where the Eocene and early Oligocene sediment is well preserved (Fig. 2) and also large multiple extensions occurred (Fig. 3a and 3b). The decompacted sediment thickness in the LSS with the routine method of backstripping is only ca. 2 km for the duration of 45–33.9 Ma (Fig. 4a), however, it reaches ca. 4 and 6 km, respectively, after both decompaction and sediment thinning correction based on the average and faults growth rates weighted strain rates using the modified technique of backstripping (Fig. 4a). The recovered sediment thickness in the LSS with the above three methods is, respectively, ca. 4, 6 and 8 km for 45–28.4 Ma (Fig. 4b), ca. 5, 7 and 7 km for 45–25.5 Ma (Fig. 4c), and ca. 6, 6 and 6 km for 45–23 Ma (Fig. 4d). The recovered huge sediment thickness in the LSS in the earlier rifting stages using the modified technique of backstripping is consistent with the large extension factors of 2–4.5 (Fig. 3b) and similar to the currently active rift, such as lake Tanganyika, the western branch of the east African rift system, where the vertical displacement exceeds 7 km and the sediment accumulation is more than 6 km (Morley, 1988). The gradually reduced sediment thickness for 45–25.5 Ma and 45–23 Ma, recovered based on the faults growth rates weighted strain rates using the modified technique of backstripping (Fig. 4c and 4d), is mainly because the previous sediment column was significantly stretched and thinned (Fig. 3a and 3b), but without enough sediment deposited (Fig. 2). After the end of rifting (23 Ma), no significant difference existed in the recovered sediment thickness among the three methods of backstripping (Fig. 4e-h).

The calculated unloaded tectonic subsidence with the three methods of backstripping (Fig. 5) have similar features as the recovered sediment thickness (Fig. 4). Using the modified technique of backstripping with the faults growth rates weighted strain rates, the present total subsidence (45–0 Ma) is ca. 1600, 2500 and 1800 m in the YBS, LSS and southern uplift, respectively (Fig. 5h). The amount of the *syn*-rift subsidence (45–23 Ma) is ca. 1000, 1500 and 400 m in the YBS, LSS and southern uplift, respectively (Fig. 7a), and that of the post-rift (23–0 Ma) increases from 500 to 1500 m in the YBS and LSS, and remains 1000–1500 m in the

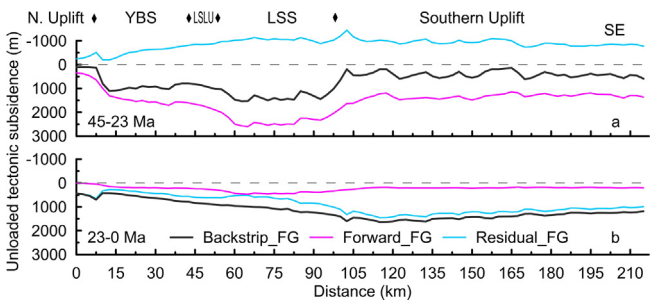

Fig. 7. The backstripped (Backstrip_FG), forward modelled (Forward_FG) and residual unloaded tectonic subsidence (Residual_FG) calculated based on the faults growth rates weighted strain rates for the *syn*-rift periods (a) and the post-rift period (b).

southern uplift (Fig. 7b). In detail, five subsidence stages are identified (Fig. 8): (1) high subsidence in the Late Eocene-Early Oligocene with the tectonic subsidence of ca. 1000, 2000 and 300 m in the YBS, LSS and southern uplift, respectively (45–28.4 Ma, Fig. 8a); (2) significant uplift in the Late Oligocene of ca. −500 m in the LSS and ca. 0 m in the YBS and southern uplift (28.4–23 Ma, Fig. 8b); (3) slow subsidence of ca. 300 m in the Early and Middle Miocene (23–11.6 Ma, Fig. 8c); (4) accelerated subsidence of ca. 1200 m mainly occurring in the southern uplift in the Late Miocene (11.6–5.5 Ma, Fig. 8d); and 5) slow subsidence of ca. 300 m focusing in the LSS since the Pliocene (5.5–0 Ma, Fig. 8e). These features are also shown in the 9 selected points (Fig. 9).

4.4. The predicted subsidence and heat flow

The predicted unloaded tectonic subsidence by the basin- and lithosphere-scale coupled finite extension model is highly dependent on the strain rate (Fig. 5). In the first rifting episodes of 45–28.4 Ma, the faults growth rates weighted strain rates are smaller than the average strain rates (Fig. 3a), thus the predicted subsidence with the weighted strain rates are smaller accordingly (Fig. 5a, 5b and 9). In the following periods, their gaps are narrowing (Fig. 5c-h and 9). With weighted strain rates, the predicted total subsidence is 1200–1900, 3000 and 1500 m in the YBS, LSS and southern uplift, respectively (Fig. 5h). For the rifting periods (45–23 Ma), the predicted subsidence is ca. 1000–1700, 2500 and 1300 m in the YBS, LSS and southern uplift, respectively (Fig. 7a). For the post-rift thermal cooling periods (23–0 Ma), it is ca. 200, 500 and 200 m in the YBS, LSS and southern uplift, respectively (Fig. 7b).

The calculated heat flow with the average strain rate and the weighted strain rates are pretty similar to each other (Fig. 2b), indicating the calculated heat flow is mainly influenced by the total strain (Fig. 3a and 3b). The measured heat flow rises progressively from 55 to 87 W/m^2 toward the SE (Wang et al., 2014; Shi et al., 2015), which equates with the predicted heat flow in the YBS, but much larger in the southern uplift (Fig. 2). By testing the thermal parameters including the thermal conductivity and heat generation, it is found that only anomalously higher parameter values can fit it. Previous study argued that the observed high heat flow can be only matched by adding the recent magmatism injection (less than 5 Ma) (Shi et al., 2017). Furthermore, our tests also give that the thermal parameters have small influence on the predicted subsidence.

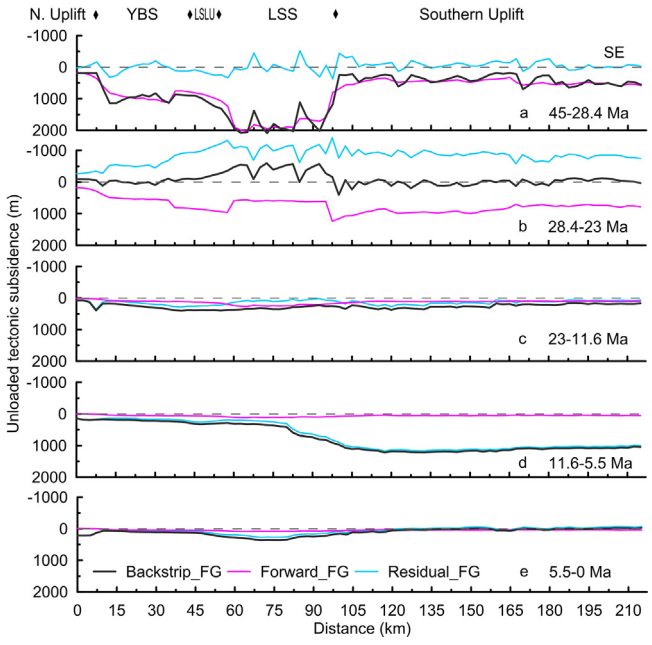

Fig. 8. The backstripped (Backstrip_FG), forward modelled (Forward_FG) and residual unloaded tectonic subsidence (Residual_FG) calculated based on the faults growth rates weighted strain rates for five stages, (a) 45–28.4 Ma, (b) 28.4–23 Ma, (c) 23–11.6 Ma, (d) 11.6–5.5 Ma, (e) 5.5–0 Ma.

4.5. The time-varying residual subsidence

The time-varying residual subsidence in Fig. 6 is derived by subtracting the predicted subsidence from the backstripped subsidence, both of which are calculated based on the faults growth rates weighted strain rates (Fig. 5). Generally, nearly zero residual subsidence exists in 45–28.4 Ma (Fig. 6a). But after ca. 28.4 Ma, ca. −1000 m residual subsidence formed until 11.6 Ma (Fig. 6b), which is apparently in the LSS and southern uplift (Fig. 6b). After 11.6 Ma, the backstripped subsidence increased considerably in the southern uplift (Fig. 5), and the present total residual subsidence is ca. 300 m in the southern uplift, but ca. −250 to −500 m in the YBS and LSS (Fig. 6c). These features are also shown in the 9 selected points (Fig. 9).

In the *syn*-rift periods (45–23 Ma), the residual subsidence is ca. −1000 m, however, in the post-rift (23–0 Ma), it is positive of ca. 300 to 1300 m increasing from the NW to SE (Fig. 7). Both the syn- and post-rift residual subsidence have large wavelengths of more than 10^2 km (Fig. 7). In detail, 5 stages of residual subsidence are identified: (1) almost zero residual subsidence in the Late Eocene to the Early Oligocene (45–28.4 Ma, Fig. 8a); (2) huge negative residual subsidence of ca. −500 to −1200 m in the Late Oligocene (28.4–23 Ma, Fig. 8b); (3) small positive residual subsidence of ca. 0–300 m in the early Miocene (23–11.6 Ma, Fig. 8c); (4) huge positive residual subsidence of ca. 300–1200 m in the Middle Miocene mainly occurring in the southern uplift (11.6–5.5 Ma, Fig. 8d); and (5) small residual subsidence of ca. 0–300 m since the Pliocene (5.5–0 Ma, Fig. 8e).

5. Discussions

5.1. The syn-rift subsidence pattern and the onset timing of the syn-rift subsidence deficit

The basement subsidence or uplift recorded by the strata preserved in sedimentary basins consists of two components: (1) the loaded subsidence generated by the filled water and sediment, and (2) the tectonic subsidence or uplift produced from the lithosphere or the underlying mantle. The amount of the tectonic subsidence or uplift is usually isolated by the method of backstripping (Sclater and Christie, 1980; Zhao et al., 2013). With the routine backstripping method, the features of the post-rift tectonic subsidence (23–0 Ma) in the QDNB have been well revealed previously (Clift and Sun, 2006; Xie et al., 2006; Zhao et al., 2013, 2018a, 2018b; Shi et al., 2017) that the basin first experienced a pretty slow subsidence in the Early and Middle Miocene (23–11.6 Ma), then followed by an accelerated subsidence since the Late Miocene (11.6–0 Ma) (Xie et al., 2006; Zhao et al., 2013). Detailed studies further found that the post-rift accelerated subsidence mainly occurred in the Late Miocene (11.6–5.5 Ma) and is much higher in the SE than the NW of the basin (Zhao et al., 2018b). But for the *syn*-rift period (45–23 Ma), some studies argued that the subsidence was high (Zhao et al., 2013, 2018b), while others suggested that it is huge deficient (Shi et al., 2017; Zhao et al., 2018a). With the modified technique of backstripping, we can not only give the similar subsidence features of the post-rift period (Fig. 8) as

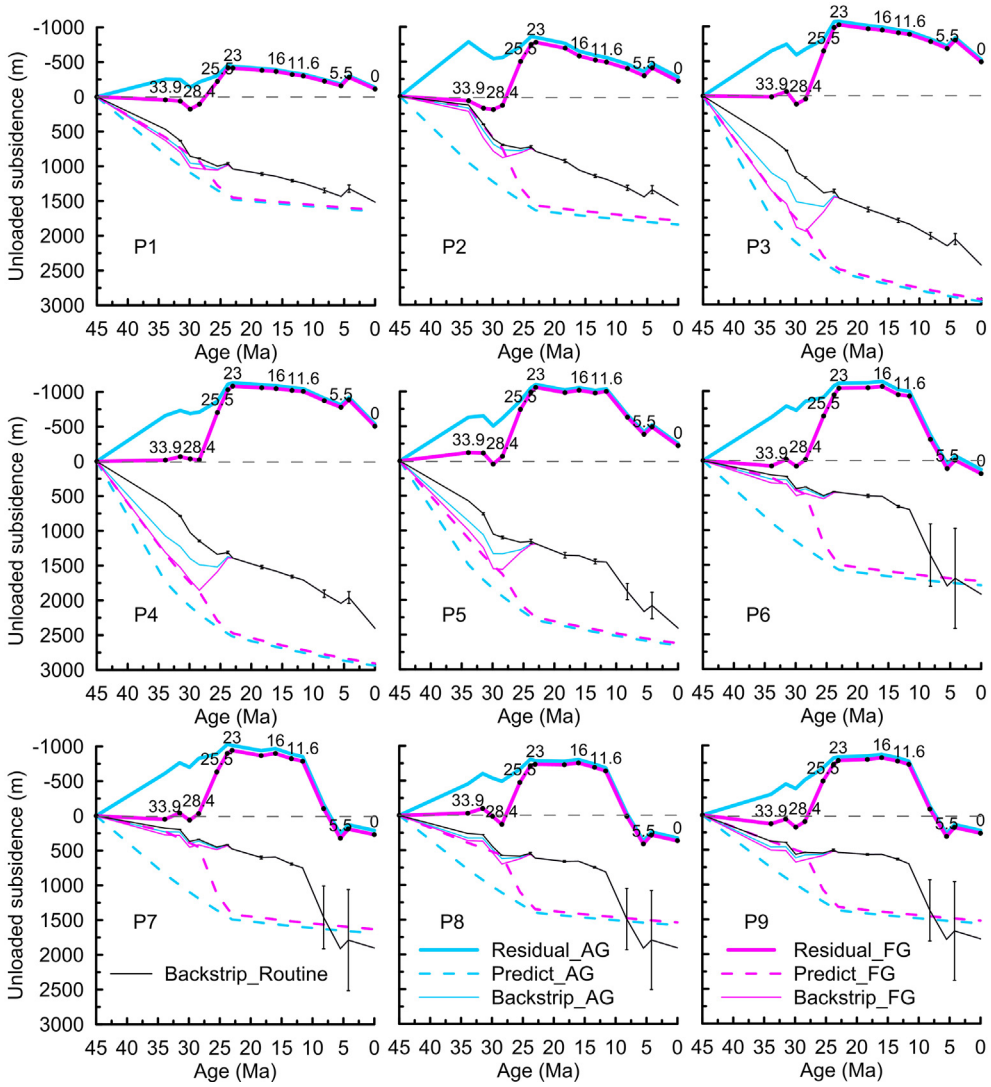

Fig. 9. Detailed subsidence analysis of the 9 selected points along line 1 (see locations in Fig. 2) for 16 sequence boundaries (45, 33.9, 31.5, 29.9, 28.4, 25.5, 23.8, 23, 18.3, 16, 13.4, 11.6, 8.2, 5.5, 4.2, and 0 Ma). The faults growth rates weighted strain rates are used to calculate the backstripped subsidence (Backstrip_FG), the forward modelled subsidence (Predict_FG), and the residual subsidence (Residual_FG). By comparison, the average strain rates are used to calculate the backstripped subsidence (Backstrip_AG), the forward modelled subsidence (Predict_AG), and the residual subsidence (Residual_AG). Meanwhile, the backstripped subsidence using the routine method of backstripping (Backstrip_Routine) is also present. The vertical bars are the uncertainties in water depth.

previous studies, but can clearly show two stages of tectonic subsidence/uplift in the *syn*-rift period: the high subsidence in the Late Eocene-Early Oligocene (45–28.4 Ma, Fig. 8a), and the significant uplift in the Late Oligocene (28.4–23 Ma, Fig. 8b).

The backstripped tectonic subsidence probably consists of both the lithospheric isostatic subsidence and the mantle viscous flow induced transient dynamic topography. For rifted basins, the isostatic subsidence is mainly contributed by the lithospheric thinning and thermal cooling (Mckenzie, 1978; Jarvis and McKenzie, 1980; Kusznir and Ziegler, 1992). In the QDNB, much work was carried out to compare the backstripped tectonic subsidence with the predicted subsidence by the lithospheric stretching models to explore the timing, amount and mechanism of the residual subsidence between them (Xie et al., 2006; Zhao et al., 2013, 2018a; Shi et al., 2017). In forward predicting the basement subsidence, three methods were usually used to obtain the strain rates (or extension factors): (1) Calculate the extension factors from faults heaves and predict the subsidence on basis of the flexural cantilever model, which showed that the predicted post-rift subsidence is much less than backstripped (Clift et al., 2002; Davis and Kusznir, 2004) and the faults derived extension factor is also smaller than the whole crust (Davis and Kusznir, 2004). It has been proved that the extension factor derived this way could be significantly underestimated due to the unresolved subseismic faulting (Walsh et al., 1991), and the unrecognized polyphase and top basement faulting (Reston, 2009). (2) Inverse strain rates from the *syn*-rift tectonic subsidence and predicted the post-rift subsidence with a finite extension model. It also showed that the predicted post-rift subsidence is less than the backstripped subsidence and the residual subsidence is ca. 300 to 1400 m increasing from the NW shelf to the SE deep water after ca. 11.6 Ma (Xie et al., 2006; Zhao et al., 2013, 2018b). Obviously, the strain rates calculated this way are subsidence dependent. However, detailed subsidence analysis (Shi et al., 2017; Zhao et al., 2018a) suggested that the *syn*-rift subsidence was significantly insufficient compared with the crustal thinning, and the extension factors estimated from the *syn*-rift subsidence is considerably less than the whole crust (Zhao et al., 2013). (3) Calculate the average strain rates by dividing the total strain (whole crustal extension factor) by the duration of the *syn*-rift period, and predict the subsidence based on a finite extension

model (Shi et al., 2017; Zhao et al., 2018a), which gave that the predicted subsidence is less than backstripped in the post-rift, but higher in the *syn*-rift (Shi et al., 2017; Zhao et al., 2018a). The strain rates are subsidence independent and can be used to predict both the syn- and post-rift subsidence, however, the average strain rate is not in accordance with the multiple rifting background in the South China margin (Ru and Pigott, 1986; Clift et al., 2001). Overall, problems still exist in the current methods to obtain the time-varying strain rates and to forward predict the syn- and post-rift basement subsidence accurately. Thus the exact time, amount and mechanism of the residual subsidence from the syn- to post-rift periods are still unclear to us. Here, for the first time, the faults growth rates weighted strain rates are proposed (Fig. 3a), which are subsidence independent, and also consistent with the multiple rifting background. Thus the subsidence predicted based on the weighted strain rates here can be more reasonable than ever (Fig. 5). By subtracting the predicted subsidence from the backstripped on basis of the modified technique of backstripping (Fig. 5), the residual subsidence is obtained (Fig. 6), the amount of which is ca. −1000 m in the *syn*-rift period (45–23 Ma, Fig. 7a), but positive of ca. 300 to 1300 m increasing from the NW to SE in the post-rift period (23–0 Ma, Fig. 7b). Furthermore, the wavelengths of the opposite syn- and post-rift residual subsidence are both larger than 10^2 km (Fig. 7). Detailed analysis further show that the *syn*-rift subsidence was deficient (negative residual subsidence) and the subsidence deficit initiated at ca. 28.4 Ma (Figs. 6, 8 and 9). The post-rift subsidence is anomalous high (positive residual subsidence), and the excess subsidence started to form at ca. 11.6 Ma mainly in the southern uplift (Figs. 6, 8 and 9).

5.2. The time-varying dynamic topography due to deep mantle upwelling

The time-varying residual subsidence with its exact timing, amplitude and wavelength (Figs. 6–9) provides an unprecedented opportunity to explore its mechanism. The post-rift excess subsidence has been widely studied in the South China Sea region, which was found to occur at ca. 11.6 Ma in the Yinggehai Basin and QDNB (Xie et al., 2006; Zhao et al., 2013, 2018b; Shi et al., 2017), at ca. 21–23 Ma in the Pearl River Mouth Basin (Clift et al., 2015), and at ca. 17 Ma in the Reed Bank area (Ding et al., 2015). Various mechanisms were also proposed, including that within the lithosphere and that from the underlying deep mantle. The lithospheric mechanisms involve the depth-dependent lithospheric stretching (Davis and Kusznir, 2004; Lei et al., 2013), the post-rift crust thinning (Zhao et al., 2013), the lower crust flow (Clift et al., 2015), and the magmatic intrusion (Xie et al., 2006; Shi et al., 2017). The underlying deep mantle mechanisms involve the small-scale mantle convection due to ocean spreading (Ding et al., 2015; Zhao et al., 2018b), the mantle flow driven by subduction (Xie et al., 2006), and the influx of warmer asthenosphere and a small-scale thermal upwelling (Shi et al., 2017). Combined with previous studies, we conclude that the lithospheric mechanisms cannot be the main cause of the time-varying residual subsidence in the QDNB (Figs. 6–9). Specifically, the post-rift accelerated subsidence started at ca. 11.6 Ma, not immediately following the end of *syn*-rift period (23 Ma, Figs. 6, 8 and 9), implying the impossibility of the depth-dependent lithospheric stretching (Davis and Kusznir, 2004; Lei et al., 2013). The spatially non-coincidence of the post-rift huge sediment in the LSS and the accelerated subsidence in the southern uplift (Figs. 4 and 5) (Zhao et al., 2015b, 2018b), suggests that the basin-widely sediment-induced lower crustal flow was unlikely to occur (Clift et al., 2015). The dramatic reduction in the faults numbers and activities in the post-rift period (Fig. 2 and Table 1) (Zhao et al., 2018b) also precludes the post-rift crustal stretching (Zhao et al., 2013). Inspired by the similar large wavelengths and km-scale amplitudes of the *syn*-rift deficient subsidence (negative residual subsidence) and the post-rift excess subsidence (positive residual subsidence) (Fig. 7), it is inferred that the *syn*-rift subsidence deficit and the post-rift excess subsidence are probably genetically linked and caused by a transient dynamic topography induced by deep mantle upwelling, which buffered the *syn*-rift subsidence and transferred it to the post-rift period.

Strong mantle upwelling in the South China Sea region has been widely argued by the geochemical analysis and the geophysical investigations (Montelli et al., 2006; Wang et al., 2013; Xia et al., 2016; Yan et al., 2018). Geochemical studies demonstrated that, in the late Cenozoic, extensive and voluminous OIB-type intraplate volcanism outcropped in the Southeast Asia around the QDNB (Xu et al., 2012; Wang et al., 2013), including the continental flood basalts in the Leizhou–Hainan area (age of ca. 13–0 Ma with a peak age from late Pliocene to middle Pleistocene) (Wang et al., 2012; Xu et al., 2012), in the nearby Indochina peninsula (age of ca. 17–0 Ma) (Hoang and Flower, 1998), and the seamount basalts in the East South China Sea basin (age of ca. 7.9–3.8 Ma) (Yan and Shi, 2008) and the Northwest South China Sea basin (ca. 23.8 Ma) (Li et al., 2015). Geochemical analyses on these basalts suggest a high mantle potential temperature of ca. 1440–1660℃, ca. 100–300℃ warmer than at the onset of rifting (Hoang and Flower, 1998; Wang et al., 2012; Yang et al., 2019). Geophysical study also found the present mantle transition zone beneath the Leizhou–Hainan area is ca. 20–50 km thinner than global average value, indicating the mantle potential temperature is ca. 180–380℃ higher than normal (Wang and Huang, 2012; Huang et al., 2015; Wei and Chen, 2016). These extensive OIB-type volcanism and high mantle potential temperature was usually thought to be linked with a hot plume originated from the lower mantle (Wang et al., 2013; Yan et al., 2018). Geophysical investigations also revealed a SE dipping low-velocity zone beneath the Leizhou–Hainan area, to the north of QDNB (Huang and Zhao, 2006; Lei et al., 2009; Xia et al., 2016), which was shown to extend from the upper mantle (Lei et al., 2009), the mid-mantle (Montelli et al., 2006) to the lower mantle (Zhao, 2007; Xia et al., 2016), and was termed as the Hainan plume (Montelli et al., 2006; Zhao, 2007; Lei et al., 2009; Xia et al., 2016). Further study showed that the lower mantle-rooted Hainan plume is rising at a rate of more than 1 cm/yr (Wang et al., 2013), and was suggested to link with the sinking and pushing of the circular active subducted slabs by geodynamical modelling (Zhang and Li, 2018). However, the diffuse igneous provinces (Hoang and Flower, 1998) and the broad upper mantle low seismic velocity (Xia et al., 2016) in the South China Sea region are inconsistent with a classical fixed narrow thermal plume that originated from the core-mantle boundary (Campbell and Davies, 2006), which were thus alternatively explained by broad mantle upwelling in the form of subduction-induced mantle return flows at greater depths (Lin et al., 2019). No matter whether a mantle plume in a classic sense exist, the deep mantle upwelling seems rigorous in the South China Sea region. However, when and how the deep mantle upwelling influences the QDNB is unknown.

Constrained by the time-varying residual subsidence in the QDNB, the onset timing of the negative residual subsidence (Figs. 6, 8 and 9) gives exactly that the deep hot mantle upwelling started to influence the basin at ca. 28.4 Ma, which continued into the middle Miocene and decayed at ca. 11.6 Ma (Figs. 6, 8 and 9). The starting time is consistent with the rapid uplift of the Hainan Island in the Late Oligocene (Shi et al., 2011), the significant uplift of the south China margin at ca. 28.5 Ma (Li et al., 2005) and the modelled dynamic uplift in the study area (Xie et al., 2006). Furthermore, the ca. 23.8 Ma OIB-type volcanism outcropped in the NW South China Sea basin (Li et al., 2015) is probably the earliest eruption after ca. 5 Ma the initial mantle upwelling (Campbell,

2005). However, the exactly locations of the deep mantle upwelling in the South China Sea region still cannot be well defined on basis of one seismic line. Here we only give a simple diagram to explain the time-varying residual subsidence in the QDNB linked to the deep mantle upwelling (Fig. 10) according to the results (Figs. 6, 8 and 9) and previous geophysical investigation (Xia et al., 2016). Under the active semi-circular subduction, the deep hot mantle is thought to upwell beneath the central QDNB at ~ 28.4 Ma (Fig. 10a). Then most of the hot mantle materials were attracted to flow southward to the stretched continent in the QDNB, the Phu Khanh Basin and the locations for future breakup of the SW South China Sea basin, yielding extensive secondary edge-driven mantle flows due to the inhomogeneous crust thickness, but little magmatic eruption in the Hainan Island and the QDNB (Fig. 10a). The mantle flow, secondary edge-driven flow and high mantle temperature beneath the QDNB together provided a transient dynamic uplift to buffer the subsidence and form the huge *syn*-rift subsidence deficit in the Late Oligocene (28.4–23 Ma) (Figs. 8 and 9). The initial surface uplift was also likely to precipitate considerable continental extension, in consistence with the strong fault activities in the Late Oligocene (Table 1 and Fig. 3) (Hill, 1991) and the development of detachment faults in the central QDNB (Lei et al., 2020). Subsequently, the hot mantle materials continued to flow southward through the QDNB to the spreading ridge of the SW South China Sea basin (ca. 23–16 Ma) (Briais et al., 1993; Li et al., 2014), and the ongoing rifting Phu Khanh Basin until ca. 12–10.5 Ma (Savva et al., 2013), thus the QDNB still shows a persistently low subsidence or minor uplift in 23–11.6 Ma (Figs. 8 and 9), leading to shallow-water platform carbonates widely developed and exposed (Ma et al., 2011; Franke et al., 2014). The strong interaction of the southwards flow mantle with the stretched continental margin and the spreading ridge (Fig. 10a) has been recorded by the mid-ocean ridge basalt in the SW South China Sea basin (Zhang et al., 2018). Since the Late Miocene, as the margin stopped rifting and seafloor spreading, the deep hot mantle upwelling beneath the QDNB begun to decay and return its position back directly below the central QDNB (Fig. 10b). Thus in the QDNB, the loss of the dynamic support and the thermal cooling of the deep hot mantle finally formed an episode of rapid subsidence in 11.6–0 Ma, especially apparently in the southern uplift (Fig s. 8, 9 and 10b). Moreover, after ca. 11.6 Ma, strong mantle upwelling probably occurred beneath the present Leizhou–Hainan area to form ca. 7000 km^2 basaltic lava flow (age of ca. 13–0 Ma with a peak age from the late Pliocene to middle Pleistocene) (Wang et al., 2012; Xu et al., 2012) (Fig. 10b).

6. Conclusions

In the hyper-extended Qiongdongnan Basin, a detailed analysis was conducted on the time-varying residual subsidence derived by subtracting the predicted subsidence from the backstripped subsidence along a new seismic line. For the first time, a method to calculate the time-varying strain rates is proposed by utilizing the faults growth rates as weight to allocate the total strain (whole crust extension factor). A forward prediction is done on the subsidence with a basin- and lithosphere-scale coupled finite extension model, and a modified technique of backstripping is given to obtain the backstripped subsidence by invoking the strain rates to eliminate the effects of later episodes of rifting on earlier sediment thickness. The residual subsidence in the *syn*-rift period (45–23 Ma) is negative of ca. −1000 m initiating at 28.4 Ma, but positive of ca. 300 to 1300 m increasing southeastwards and starting at 11.6 Ma in the post-rift period (23–0 Ma), inferring that the *syn*-rift subsidence is deficient and commenced at 28.4 Ma, but the post-rift subsidence is anomalously excess and appeared after 11.6 Ma mainly in the southern uplift. Their wavelengths are both larger than 10^2 km, indicating a deep origin. Combined with previous studies, it is inferred that the opposite residual subsidence during the syn- and post-rift periods with similar large wavelengths and km-scale amplitudes are the results of transient dynamic topography induced by deep mantle upwelling beneath the central QDNB, which started to influence the basin at ca. 28.4 Ma, continued into the Middle Miocene, and decayed at ca. 11.6 Ma. After ca. 11.6 Ma, strong mantle upwelling probably occurred beneath the Leizhou–Hainan area to form vast basaltic lava flow.

Declaration of Competing Interest

The authors declare that they have no known competing financial interests or personal relationships that could have appeared to influence the work reported in this paper.

Acknowledgements

We thank Editorial Advisor Prof. M. Santosh and Associate Editor Dr. Masaki Yoshida for their great efforts in handling the manuscript and the anonymous reviewers for their constructive and detailed comments. We are grateful to CNOOC for providing the seismic profiles. This research was supported by the Laboratory for Marine Mineral Resources, Qingdao National Laboratory for Marine Science and Technology (NO. MMRKF201805), by CAS

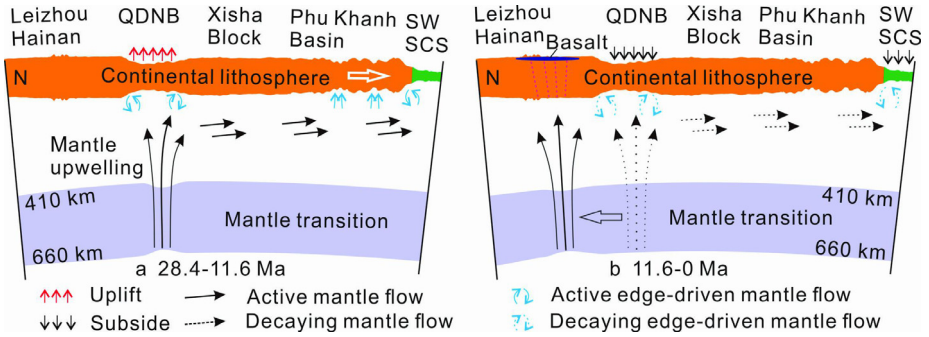

Fig. 10. Simple schematic diagrams to explain the time-varying residual subsidence in the QDNB linked to the deep hot mantle upwelling induced dynamic topography. (a) Deep hot mantle material upwelling beneath the central QDNB started at ca. 28.4 Ma, and then was attracted to flow southward to the stretched continent and seafloor spreading ridge. The mantle flow, the secondary edge-driven flow and the high mantle temperature beneath the QDNB together provided a transient dynamic support to buffer the subsidence to form a huge *syn*-rift subsidence deficit during 28.4–23 Ma and a significantly low subsidence in the early post-rift period of 23–11.6 Ma. (b) During 11.6–0 Ma, as the margin stopped rifting and seafloor spreading, the deep hot mantle upwelling beneath the QDNB begun to decay and return its position back directly below the central QDNB. Thus in the QDNB, the loss of the dynamic support and the thermal cooling of the deep hot mantle finally yielded a rapid subsidence in the late post-rift period (11.6–0 Ma), especially apparently in the southern uplift. Moreover, after ca. 11.6 Ma, strong mantle upwelling probably occurred beneath the present Leizhou-Hainan area to form the extensive basaltic lava flow.

Youth Innovation Promotion Association, by Key Special Project for Introduced Talents Team of Southern Marine Science and Engineering Guangdong Laboratory (Guangzhou) (GML2019ZD0205), by Guangzhou Municipal Science and technology program (NO. 201904010285), by K.C. Wong Education Foundation (NO. GJTD-2018-13), by Key Laboratory of Marine Mineral Resources, Ministry of Natural Resources (NO. KLMMR-2018-B-06), by Innovation Academy of South China Sea Ecology and Environmental Engineering, Chinese Academy of Sciences (NO. ISEE2018PY02), and by National Natural Science Foundation of China (NO. 42076077).

Data availability statement

The sequence boundaries data derived from seismic Line 1 and the Moho and crustal thickness data obtained from the seismic interpretation and the gravity modelling are available at FigShare (https://figshare.com/articles/Data_Seismic_line_1/12470189), the gravity anomaly data are available through Sandwell et al. (2014), and the heat flow data is available through Wang et al. (2014) and Shi et al. (2015).

References

Briais, A., Patriat, P., Tapponnier, P., 1993. Updated Interpretation of Magnetic-Anomalies and Sea-Floor Spreading Stages in the South China Sea - Implications for the Tertiary Tectonics of Southeast-Asia. J. Geophys. Res.: Solid Earth 98, 6299–6328.

Brown, B.J., Muller, R.D., Struckmeyer, H.I.M., 2001. Anomalous tectonic subsidence of the Southern Australian Passive Margin: Response to cretaceous dynamic topography or differential lithospheric stretching?. PESA Eastern Aust. Basins Sympos., 563–569

Campbell, I.H., 2005. Large igneous provinces and the mantle plume hypothesis. Elements 1 (5), 265–269.

Campbell, I.H., Davies, G.F., 2006. Do mantle plumes exist?. Episodes 29 (3), 162–168.

Christensen, N.I., Mooney, W.D., 1995. Seismic Velocity Structure and Composition of the Continental-Crust - a Global View. J. Geophys. Res.: Solid Earth 100 (B6), 9761–9788.

Clift, P., Lin, J., 2001. Preferential mantle lithospheric extension under the South China Margin. Mar. Petrol. Geol. 18 (8), 929–945.

Clift, P., Lin, J., Barckhausen, U., 2002. Evidence of low flexural rigidity and low viscosity lower continental crust during continental break-up in the South China Sea. Mar. Petrol. Geol. 19 (8), 951–970.

Clift, P., Lin, J., Party, O.L.S., 2001. Patterns of extension and magmatism along the continent-ocean boundary, South China margin. Geol. Soc., London, Spec. Publ. 187, 489–510.

Clift, P.D., Brune, S., Quinteros, J., 2015. Climate changes control offshore crustal structure at South China Sea continental margin. Earth Planet. Sci. Lett. 420, 66–72.

Clift, P.D., Sun, Z., 2006. The sedimentary and tectonic evolution of the Yinggehai-Song Hong basin and the southern Hainan margin, South China Sea: Implications for Tibetan uplift and monsoon intensification. J. Geophys. Res. 111, 1–28.

Cullen, A., Reemst, P., Henstra, G., Gozzard, S., Ray, A., 2010. Rifting of the South China Sea: new perspectives. Petrol. Geosci. 16 (3), 273–282.

Davis, M., Kusznir, N., 2004. In: Depth-dependent lithospheric stretching at rifted continental margins. Columbia University Press, New York, pp. 92–137.

Ding, W., Li, J., Dong, C., Fang, Y., 2015. Oligocene-Miocene carbonates in the Reed Bank area, South China Sea, and their tectono-sedimentary evolution. Mar. Geophys. Res. 36 (2-3), 149–165.

Ding, W., Sun, Z., Dadd, K., Fang, Y., Li, J., 2018. Structures within the oceanic crust of the central South China Sea basin and their implications for oceanic accretionary processes. Earth Planet. Sci. Lett. 488, 115–125.

Franke, D., Savva, D., Pubellier, M., Steuer, S., Mouly, B., Auxietre, J.-L., Meresse, F., Chamot-Rooke, N., 2014. The final rifting evolution in the South China Sea. Mar. Petrol. Geol. 58, 704–720.

Hill, R.I., 1991. Starting Plumes and Continental Break-Up. Earth Planet. Sci. Lett. 104 (2-4), 398–416.

Hoang, N., Flower, M., 1998. Petrogenesis of Cenozoic basalts from Vietnam: Implication for origins of a 'Diffuse igneous province'. J. Petrol. 39 (3), 369–395.

Huang, H., Tosi, N., Chang, S.-J., Xia, S., Qiu, X., 2015. Receiver function imaging of the mantle transition zone beneath the South China Block. Geochem. Geophy. Geosy. 16, 3666–3678.

Huang, J.L., Zhao, D.P., 2006. High-resolution mantle tomography of China and surrounding regions. J. Geophys. Res.: Solid. Earth 111, B09305. https://doi.org/10.1029/2005JB004066.

Jarvis, G.T., McKenzie, D.P., 1980. Sedimentary basin formation with finite extension rates. Earth Planet. Sci. Lett. 48 (1), 42–52.

Kusznir, N.J., Ziegler, P.A., 1992. The mechanics of continental extension and sedimentary basin formation: A simple-shear/pure-shear flexural cantilever model. Tectonophysics, 117–131.

Lei, C., Alves, T.M., Ren, J.Y., Pang, X., Yang, L.L., Liu, J., 2019. Depositional architecture and structural evolution of a region immediately inboard of the locus of continental breakup (Liwan Sub-basin, South China Sea). Geol. Soc. Am. Bull. 131, 1059–1074.

Lei, C., Alves, T.M., Ren, J., Tong, C., 2020. Rift Structure and Sediment Infill of Hyperextended Continental Crust: Insights From 3D Seismic and Well Data (Xisha Trough, South China Sea). J. Geophys. Res.: Solid. Earth 125 (5). https://doi.org/10.1029/2019JB018610.

Lei, C., Ren, J., 2016. Hyper-extended rift systems in the Xisha Trough, northwestern South China Sea: Implications for extreme crustal thinning ahead of a propagating ocean. Mar. Petrol. Geol. 77, 846–864.

Lei, C., Ren, J.Y., Tong, D.J., 2013. Geodynamics of the ocean-continent transition zone, northern margin of the South China Sea: Implications for the opening of the South China Sea. Chin. J. Geophys. 56, 1287–1299.

Lei, J., Zhao, D., Steinberger, B., Wu, B., Shen, F., Li, Z., 2009. New seismic constraints on the upper mantle structure of the Hainan plume. Phys. Earth Planet. In. 173 (1-2), 33–50.

Li, C., Liu, S.F., 2015. Cretaceous anomalous subsidence and its response to dynamic topography in the Songliao Basin. Northeast China. J. Asian Earth Sci. 109, 86–99.

Li, C.-F., Xu, X., Lin, J., Sun, Z., Zhu, J., Yao, Y., Zhao, X., Liu, Q., Kulhanek, D.K., Wang, J., Song, T., Zhao, J., Qiu, N., Guan, Y., Zhou, Z., Williams, T., Bao, R., Briais, A., Brown, E.A., Chen, Y., Clift, P.D., Colwell, F.S., Dadd, K.A., Ding, W., Almeida, I.H., Huang, X.-L., Hyun, S., Jiang, T., Koppers, A.A.P., Li, Q., Liu, C., Liu, Z., Nagai, R.H., Peleo-Alampay, A., Su, X., Tejada, M.L.G., Trinh, H.S., Yeh, Y.-C., Zhang, C., Zhang, F., Zhang, G.-L., 2014. Ages and magnetic structures of the South China Sea constrained by deep tow magnetic surveys and IODP Expedition 349. Geochem. Geophys. Geosyst. 15 (12), 4958–4983.

Li, Q., Jian, Z., Su, X., 2005. Late Oligocene rapid transformations in the South China Sea. Mar. Micropaleontol. 54 (1-2), 5–25.

Li, X.H., Li, J.B., Yu, X., Wang, C.S., Jourdan, F., 2015. Ar-40/Ar-39 ages of seamount trachytes from the South China Sea and implications for the evolution of the northwestern sub-basin. Geosci. Front. 6, 571–577.

Lin, J., Xu, Y.G., Sun, Z., Zhou, Z.Y., 2019. Mantle upwelling beneath the South China Sea and links to surrounding subduction systems. Natl. Sci. Rev. 6, 877–881.

Müller, R.D., Lim, V.S.L., Isern, A.R., 2000. Late tertiary tectonic subsidence on the northeast Australian passive margin: response to dynamic topography?. Mar. Geol. 162 (2-4), 337–352.

Ma, Y.B., Wu, S.G., Lv, F.L., Dong, D.D., Sun, Q.L., Lu, Y.T., Gu, M.F., 2011. Seismic characteristics and development of the Xisha carbonate platforms, northern margin of the South China Sea. J. Asian Earth Sci. 40, 770–783.

Mckenzie, D., 1978. Some Remarks on Development of Sedimentary Basins. Earth Planet. Sci. Lett. 40, 25–32.

Montelli, R., Nolet, G., Dahlen, F.A., Masters, G., 2006. A catalogue of deep mantle plumes: New results from finite-frequency tomography. Geochem. Geophy. Geosy. 7 (11), Q11007.

Morley, C.K., 1988. Variable Extension in Lake Tanganyika. Tectonics 7 (4), 785–801.

Nadin, P.A., Kusznir, N.J., Cheadle, M.J., 1997. Early Tertiary plume uplift of the North Sea and Faeroe-Shetland Basins. Earth Planet. Sci. Lett. 148 (1-2), 109–127.

Nissen, S.S., Hayes, D.E., 1995. Gravity, heat flow, and seismic constrains on the processes of crustal extension: Northern margin of the South China Sea. J. Geophys. Res. 100, 22477–22483.

Nissen, S.S., Hayes, D.E., Buhl, P., Diebold, J., Bochu, Y., Zeng, W., Chen, Y., 1995. Deep Penetration Seismic-Soundings across the Northern Margin of the South China Sea. J. Geophys. Res.: Solid Earth 100 (B11), 22407–22433.

Praeg, D., Stoker, M.S., Shannon, P.M., Ceramicola, S., Hjelstuen, B., Laberg, J.S., Mathiesen, A., 2005. Episodic Cenozoic tectonism and the development of the NW European 'passive' continental margin. Mar. Petrol. Geol. 22 (9-10), 1007–1030.

Qiu, N., Wang, Z., Xie, H., Sun, Z., Wang, Z., Sun, Z., Zhou, D.i., 2013. Geophysical investigations of crust-scale structural model of the Qiongdongnan Basin, Northern South China Sea. Mar. Geophys. Res. 34 (3-4), 259–279.

Reston, T.J., 2009. The extension discrepancy and syn-rift subsidence deficit at rifted margins. Petrol. Geosci. 15 (3), 217–237.

Ru, K., Pigott, J.D., 1986. Episodic rifting and subsidence in the South China Sea. AAPG Bull. 70, 1136–1155.

Rüpke, L.H., Schmalholz, S.M., Schmid, D.W., Podladchikov, Y.Y., 2008. Automated thermotectonostratigraphic basin reconstruction: Viking Graben case study. AAPG Bull. 92 (3), 309–326.

Sandwell, D.T., Müller, R.D., Smith, W.H.F., Garcia, E., Francis, R., 2014. New global marine gravity model from CryoSat-2 and Jason-1 reveals buried tectonic structure. Science 346 (6205), 65–67.

Savva, D., Meresse, F., Pubellier, M., Chamot-Rooke, N., Lavier, L., Po, K.W., Franke, D., Steuer, S., Sapin, F., Auxietre, J.L., Lamy, G., 2013. Seismic evidence of hyper-stretched crust and mantle exhumation offshore Vietnam. Tectonophysics 608, 72–83.

Sclater, J.G., Christie, P.A.F., 1980. Continental Stretching: An Explanation of the Post-Mid-Cretaceous Subsidence of the Central North Sea Basin. J. Geophys. Res. 85 (B7), 3711–3739.

Shi, X., Jiang, H., Yang, J., Yang, X., Xu, H., 2017. Models of the rapid post-rift subsidence in the eastern Qiongdongnan Basin, South China Sea: implications for the development of the deep thermal anomaly. Basin Res. 29 (3), 340–362.
Shi, X., Kohn, B., Spencer, S., Guo, X., Li, Y., Yang, X., Shi, H., Gleadow, A., 2011. Cenozoic denudation history of southern Hainan Island, South China Sea: Constraints from low temperature thermochronology. Tectonophysics 504 (1-4), 100–115.
Shi, X.B., Wang, Z.F., Jiang, H.Y., Sun, Z.P., Sun, Z., Yang, J., Yu, C.H., Yang, X.Q., 2015. Vertical variations of geothermal parameters in rifted basins and heat flow distribution features of the Qiongdongnan Basin. Chin. J. Geophys. 58, 939–952.
Su, D., White, N., McKenzie, D., 1989. Extension and subsidence of the Pearl River Mouth Basin, northern South China Sea. Basin Res. 2 (4), 205–222.
Su, M., Xie, X.-N., Jiang, T., Li, J.-L., Sun, Z.-P., Tian, S.-S., Zhang, C., He, Y.-L., Zhang, C.-M., 2011. Characteristics of S40 Boundary and its significance in Qiongdongnan Basin, Northern Continental Margin of South China Sea. Earth Sci. J. China U. Geosci. 36, 886–894.
Sun, Z., Jian, Z., Stock, J.M., Larsen, H.C., Klaus, A., Zarikian, A., A., C., Scientists, t.E., 2018. South China Sea Rifted Margin. Proceedings of the International Ocean Discovery Program, 367/368: College Station, TX (International Ocean Discovery Program).
Tang, X.Y., Hu, S.B., Zhang, G.C., Yang, S.C., Shen, H.L., Rao, S., Li, W.W., 2014. Characteristic of surface heat flow in the Pearl River Mouth Basin and its relationship with thermal lithosphere thickness. Chin. J. Geophys. 57, 1857–1867.
Theissen, S., Rupke, L.H., 2010. Feedbacks of sedimentation on crustal heat flow: New insights from the V circle divide ring Basin, Norwegian Sea. Basin Res. 22, 976–990.
Walsh, J., Watterson, J., Yielding, G., 1991. The importance of small-scale faulting in regional extension. Nature 351 (6325), 391–393.
Wang, C.Y., Huang, J.L., 2012. Mantle transition zone structure around Hainan by receiver function analysis. Chin. J. Geophys.-CH 55, 1161–1167.
Wang, X.C., Li, Z.X., Li, X.H., Li, J., Liu, Y., Long, W.G., Zhou, J.B., Wang, F., 2012. Temperature, Pressure, and Composition of the Mantle Source Region of Late Cenozoic Basalts in Hainan Island, SE Asia: a Consequence of a Young Thermal Mantle Plume close to Subduction Zones?. J. Petrol. 53, 177–233.
Wang, X.C., Li, Z.X., Li, X.H., Li, J., Xu, Y.G., Li, X.H., 2013. Identification of an ancient mantle reservoir and young recycled materials in the source region of a young mantle plume: Implications for potential linkages between plume and plate tectonics. Earth Planet. Sci. Lett. 377-378, 248–259.
Wang, Z.F., Shi, X.B., Yang, J., Huang, B.J., Sun, Z., Wang, Y.H., Jiang, H.Y., Yu, C.H., Yang, X.Q., 2014. Analyses on the tectonic thermal evolution and influence factors in the deep-water Qiongdongnan Basin. ACTA Oceanol. Sin. 33 (12), 107–117.
Watts, A.B., Stewart, J., 1998. Gravity anomalies and segmentation of the continental margin offshore West Africa. Earth Planet. Sci. Lett. 156 (3-4), 239–252.
Wei, S.S., Chen, Y.J., 2016. Seismic evidence of the Hainan mantle plume by receiver function analysis in southern China. Geophys. Res. Lett. 43 (17), 8978–8985.
Wheeler, P., White, N., 2000. Quest for dynamic topography: Observations from Southeast Asia. Geology 28, 963–966.
White, N., 1994. An inverse method for determining lithospheric strain rate variation on geological timescales. Earth Planet. Sci. Lett. 122 (3-4), 351–371.
Xia, S.H., Zhao, D.P., Sun, J.L., Huang, H.B., 2016. Teleseismic imaging of the mantle beneath southernmost China: New insights into the Hainan plume. Gondwana Res. 36, 46–56.
Xie, X., Muller, R.D., Li, S., Gong, Z., Sterinberger, B., 2006. Origin of anomalous subsidence along the Northern South China Sea margin and its relationship to dynamic topography. Mar. Petrol. Geol. 23 (7), 745–765.
Xie, X., Muller, R.D., Ren, J., Jiang, T., Zhang, C., 2008. Stratigraphic architecture and evolution of the continental slope system in offshore Hainan, northern South China Sea. Mar. Geol. 247 (3-4), 129–144.
Xu, Y.G., Wei, J.X., Qiu, H.N., Zhang, H.H., Huang, X.L., 2012. Opening and evolution of the South China Sea constrained by studies on volcanic rocks: Preliminary results and a research design. Chinese Sci. Bull. 57 (24), 3150–3164.
Yan, Q., Shi, X., 2008. Olivine chemistry of Cenozoic basalts in the South China Sea and the potential temperature of the mantle. Acta Petrol. Sin. 24, 176–184.
Yan, Q., Shi, X., Metcalfe, I., Liu, S., Xu, T., Kornkanitnan, N., Sirichaiseth, T., Yuan, L., Zhang, Y., Zhang, H., 2018. Hainan mantle plume produced late Cenozoic basaltic rocks in Thailand, Southeast Asia. Sci. Rep. 8, 2640.
Yang, F., Huang, X.L., Xu, Y.G., He, P.L., 2019. Plume-ridge interaction in the South China Sea: Thermometric evidence from Hole U1431E of IODP Expedition 349. Lithos 324-325, 466–478.
Zhang, G.L., Luo, Q., Zhao, J., Jackson, M.G., Guo, L.S., Zhong, L.F., 2018. Geochemical nature of sub-ridge mantle and opening dynamics of the South China. Earth Planet. Sci. Lett. 489, 145–155.
Zhang, N., Li, Z.X., 2018. Formation of mantle “lone plumes” in the global downwelling zone - A multiscale modelling of subduction-controlled plume generation beneath the South China Sea. Tectonophysics 723, 1–13.
Zhang, Y.F., Sun, Z., Zhou, D., Guo, X.W., Shi, X.B., Wu, X.J., Pang, X., 2008. Stretching characteristics and its dynamic significance of the northern continental margin of South China Sea. Sci. China Ser. D 51 (3), 422–430.
Zhao, D., 2007. Seismic images under 60 hotspots: Search for mantle plumes. Gondwana Res. 12 (4), 335–355.
Zhao, Z., Sun, Z., Liu, J., Pérez-Gussinyé, M., Zhuo, H., 2018a. The continental extension discrepancy and anomalous subsidence pattern in the western Qiongdongnan Basin, South China Sea. Earth Planet. Sci. Lett. 501, 180–191.
Zhao, Z.X., Sun, Z., Sun, L.T., Wang, Z.F., Sun, Z.P., 2018b. Cenozoic tectonic subsidence in the Qiongdongnan Basin, northern South China Sea. Basin Res. 30, 269–288.
Zhao, Z.X., Sun, Z., Wang, Z.F., Sun, Z.P., 2015a. The mechanics of continental extension in Qiongdongnan Basin, northern South China Sea. Mar. Geophys. Res. 36 (2-3), 197–210.
Zhao, Z.X., Sun, Z., Wang, Z.F., Sun, Z.P., Liu, J.B., Wang, Z.W., Sun, L.T., 2013. The dynamic mechanism of post-rift accelerated subsidence in Qiongdongnan Basin, northern South China Sea. Mar. Geophys. Res. 34 (3-4), 295–308.
Zhao, Z.X., Sun, Z., Wang, Z.F., Sun, Z.P., Liu, J.B., Zhang, C.M., 2015b. The high resolution sedimentary filling in Qiongdongnan Basin, Northern South China Sea. Mar. Geol. 361, 11–24.